LAWRENCE
LIVERMORE
NATIONAL
LABORATORY

LLNL-JRNL-649079

Interfacial dislocation motion and interactions in single-crystal superalloys

B. Liu, D. Raabe, F. Roters, A. Arsenlis

January 31, 2014

Acta Materialia

Disclaimer

Interfacial dislocation motion and interactions in single-crystal superalloys

B. Liu[1,2,*], D. Raabe[2], F. Roters[2], A. Arsenlis[1]

[1]Lawrence Livermore National Laboratory, Livermore, CA 94550, USA
[2]Max-Planck-Institut für Eisenforschung, 40237 Düsseldorf, Germany
[*]Corresponding author: bingliu@llnl.gov (B. Liu)

January 28, 2014

Abstract

The early stage of high temperature low stress creep in single-crystal superalloys is characterized by the rapid development of interfacial dislocation networks. Although interfacial motion and dynamic recovery of these dislocation networks have long been expected to control the subsequent creep behavior, direct observation and hence in-depth understanding of such processes has not been reached. Incorporating recent developments of discrete dislocation dynamics models, we simulate interfacial dislocation motion in the channel structures of single-crystal superalloys, and investigate how interfacial dislocation motion and dynamic recovery are affected by interfacial dislocation interactions and lattice misfit. Different types of dislocation interactions are considered: self, collinear, coplanar, Lomer junction, glissile junction and Hirth junction. The simulation results show that strong dynamic recovery occurs due to the short-range reactions of collinear annihilation and Lomer junction formation. The misfit stress is found to induce and accelerate dynamic recovery of interfacial dislocation networks involving self-interaction and Hirth junction formation, but slow down the steady interfacial motion of coplanar and glissile junction forming dislocation networks. The insights gained from these simulations on high temperature low stress creep of single-crystal superalloys will also be discussed.

Keywords: Dislocation dynamics; superalloys; high temperature low stress creep; interfacial dislocation motion; dislocation interactions

1 Introduction

Single-crystal superalloys are used as turbine blade materials because of their excellent creep resistance during the operation of gas turbines in aircraft and power engines. The microstructure

of these alloys consists of γ matrix (face centered cubic) containing a high volume fraction of cuboidal γ' particles ($L1_2$ lattice). Creep deformation in these structures exhibits three regimes: a low temperature and high stress regime (e.g. $750\,^{\circ}$C, 750 MPa), where plastic strain is accumulated by $\langle 1\,1\,2\rangle$ dislocation ribbons cutting of the γ' precipitates [1, 2]; an intermediate temperature and stress regime (e.g. $900\,^{\circ}$C, 450 MPa), where plastic deformation occurs by Orowan bypassing of $1/2\,\langle 0\,1\,1\rangle$ dislocations through the γ matrix channels [3, 4]; and a high temperature and low stress regime (e.g. $1100\,^{\circ}$C, 137 MPa), where plastic deformation initializes easily as the grown-in $1/2\,\langle 0\,1\,1\rangle$ dislocations glide in the horizontal channels [5–7], proceeds slowly by the motion of $1/2\,\langle 0\,1\,1\rangle$ dislocations along the interfaces [8–10], and eventually accelerates via $\langle 1\,0\,0\rangle$ superdislocations cutting of the γ' precipitates [11, 12].

Interfacial dislocation motion and interactions occur in the high temperature and low stress regime. These interfacial dislocations are generated by the glide of grown-in dislocations driven jointly by the applied stress and misfit stress in the horizontal channels [13–15]. As more dislocations are deposited on the interface, the internal stresses associated with the interfacial dislocation networks soon become high enough to prevent the further propagation of the grown-in dislocations, and thus end primary creep [5, 16, 17]. Interfacial dislocation motion, by a combination of glide and climb, becomes the main deformation process during secondary creep that constitutes the majority of the superalloy's creep life [9, 10, 18, 19].

The objective of this work is to investigate how interfacial dislocation motion in the γ/γ' structure is affected by long-range and short-range dislocation interactions in interfacial dislocation networks using discrete dislocation dynamics (DDD) simulations. Three-dimensional DDD models [20–25] are robust tools to study elementary dislocation interactions [26–28], and the strengthening effect of dislocation interactions in nano-scale metallic multilayered composites [29], micro-scale plasticity [30–32], and coarse-grained crystals at low-angle grain boundaries [33, 34]. The present work is focused on the role of interfacial dislocation interactions during high temperature creep of single-crystal superalloys. In previous studies [26–29, 31–34], dislocation interactions were generally found to contribute to material strength and cause strain hardening. In this work, we show that interfacial dislocation interactions may also induce dynamic recovery, which relieves internal stress and leads to creep softening. Although dynamic recovery has long been assumed to occur during secondary creep of single-crystal superalloys [5, 9, 10, 18, 19], direct observation and hence in-depth understanding of such processes has not been reached. In the γ phase matrix channels, positive and negative dislocations are forced by the external stresses onto opposite interfaces, so that dynamic recovery does not proceed as in pure metals where dislocations of opposite signs directly meet and annihilate. Our simulations of interfacial dislocation motion and interactions will cast light on the recovery mechanisms during high temperature low stress creep in these channel structures.

We will first introduce our model to simulate interfacial dislocation motion and interactions in the γ/γ' structure, which includes model modifications that enable dislocation climb driven by mechanical and chemical forces, incorporates the antiphase boundary back-driving force in the precipitates, and considers the biaxial misfit stresses in the matrix channels. The simulations of interfacial dislocation motion during creep are next presented, which consider different initial configurations, namely, mixed dislocations, edge dislocations, and dislocation networks involving different types of dislocation interactions (self, collinear, coplanar, Lomer junction, glissile

junction and Hirth junction). In each case, the role of the misfit stresses is also investigated by running two separate simulations with the misfit stresses in the model being switched on and off, respectively. The insights gained from these simulations on high temperature low stress creep in single-crystal superalloys will be finally discussed and summarized.

2 Simulation method

Dislocations climb through emission and adsorption of vacancies at jogs. Under the condition of high temperature and low stress, the jog density is high enough that each point along the dislocation line may act as a source or sink of vacancies, and the vacancy concentration is approximately uniform along the dislocation core [35]. The velocity of dislocation climb is then controlled by vacancy diffusion [35–42]:

$$V_c = \frac{2\pi\Omega D_v c_0 F_c}{b^2 \ln\left(R/b\right) k_B T}, \tag{1}$$

where D_v is the vacancy diffusion coefficient, c_0 is the equilibrium vacancy concentration, F_c is the climb force, Ω is the atomic volume, b is the magnitude of the Burgers vector, R is a distance from the dislocation core over which the vacancy concentration reaches its average value in the sample, k_B is Boltzmann's constant, and T is the absolute temperature.

A drag relation between the climb force and velocity can be derived from Eq. (1):

$$V_c = \frac{F_c}{B_c},\ B_c = \frac{b^2 \ln\left(R/b\right) k_B T}{2\pi\Omega D_v c_0}, \tag{2}$$

where the drag coefficient B_c is a function of the vacancy diffusion coefficient D_v, the equilibrium vacancy concentration c_0, and the temperature T. It is worth mentioning that a similar climb force-velocity drag relation has also been derived in the case of low jog density (source/sink controlled climb) [43].

The climb motion of dislocations can be described in a drag-type relation similar to the glide motion, which allows dislocation dynamics models to handle dislocation glide and climb in the same framework [25, 39, 41, 43–45].

We use the ParaDiS DDD code [25], which defines the nodal force and velocity in a drag-type relation:

$$\boldsymbol{F}_i = \frac{1}{2}\sum_j \|\boldsymbol{l}_{ij}\| \boldsymbol{B}_{ij} \boldsymbol{V}_i, \tag{3}$$

where $\boldsymbol{F}_i$ is the force on node i, j is a node connected to i through a line segment $\boldsymbol{l}_{ij}$, $\boldsymbol{B}_{ij}$ is the drag tensor (inverted mobility tensor) for segment $\boldsymbol{l}_{ij}$, and $\boldsymbol{V}_i$ is the calculated nodal velocity. The drag tensor $\boldsymbol{B}$ enforces spatial constraints on the dislocation motion in face centered cubic (FCC) crystals according to:

$$\boldsymbol{B} = \begin{cases} B_g\left(\boldsymbol{m}\otimes\boldsymbol{m}\right) + B_c\left(\boldsymbol{n}\otimes\boldsymbol{n}\right) + B_l\left(\boldsymbol{t}\otimes\boldsymbol{t}\right) & \boldsymbol{n} \parallel \langle 111\rangle \\ B_c\boldsymbol{I} + \left(B_l - B_c\right)\left(\boldsymbol{t}\otimes\boldsymbol{t}\right) & \boldsymbol{n} \nparallel \langle 111\rangle \end{cases} \tag{4}$$

where the drag coefficient B_g controls dislocation glide on the glide plane and perpendicular to the dislocation line, B_c defines dislocation climb along the glide plane normal $\boldsymbol{n}$, and B_l is the drag coefficient associated with moving a node along its line direction $\boldsymbol{t}$.

The FCC mobility law in the ParaDiS code [25, 46] defined through Eq. (3) and (4) was designed primarily for dislocation glide on $\{1\,1\,1\}$ planes, and B_c was set large enough to prevent glide on non-$\{1\,1\,1\}$ planes and climb in general. As dislocations lose their initial glide planes in a three-dimensional DDD simulation incorporating dislocation climb, e.g. activation of a Bardeen-Herring source [38], glide on $\{1\,1\,1\}$ and non-$\{1\,1\,1\}$ planes should be treated in a similar fashion [39]. In this work, we thus modified the non-$\{1\,1\,1\}$ drag tensor to be the same as the $\{1\,1\,1\}$ drag tensor:

$$\boldsymbol{B} = B_g\left(\boldsymbol{m}\otimes\boldsymbol{m}\right) + B_c\left(\boldsymbol{n}\otimes\boldsymbol{n}\right) + B_l\left(\boldsymbol{t}\otimes\boldsymbol{t}\right), \quad \boldsymbol{n} \parallel \langle 111\rangle \ \cup \ \boldsymbol{n} \nparallel \langle 111\rangle . \tag{5}$$

The nodal force in the model is calculated from the forces exerted on the segments that the node connects:

$$\boldsymbol{F}_i = \sum_j \boldsymbol{f}_{ij}. \tag{6}$$

The segment force $\boldsymbol{f}_{ij}$ has multiple sources:

$$\boldsymbol{f}_{ij} = \boldsymbol{f}_{ij}^{core} + \boldsymbol{f}_{ij}^{elastic} + \boldsymbol{f}_{ij}^{external} + \boldsymbol{f}_{ij}^{osmotic} + \boldsymbol{f}_{ij}^{APB} + \boldsymbol{f}_{ij}^{misfit}. \tag{7}$$

$\boldsymbol{f}_{ij}^{core}$ is the line tension force to minimize the dislocation core energy by reducing the segment length and rotating the segment towards lower energy orientation. $\boldsymbol{f}_{ij}^{elastic}$ is the elastic force due to the stress field of the dislocation network. $\boldsymbol{f}_{ij}^{external}$ is the external force due to the remotely applied stress. $\boldsymbol{f}_{ij}^{osmotic}$ is the osmotic force due to vacancy depletion or supersaturation. $\boldsymbol{f}_{ij}^{APB}$ is the antiphase boundary (APB) back-driving force to prevent dislocation cutting of the γ' precipitates. $\boldsymbol{f}_{ij}^{misfit}$ is the force due to the presence of misfit stress in the γ/γ' structures. The explicit forms of $\boldsymbol{f}_{ij}^{core}$, $\boldsymbol{f}_{ij}^{elastic}$, and $\boldsymbol{f}_{ij}^{external}$ are given in Ref. [25]. The expressions for $\boldsymbol{f}_{ij}^{osmotic}$, $\boldsymbol{f}_{ij}^{APB}$, and $\boldsymbol{f}_{ij}^{misfit}$ are listed below.

The osmotic force is in the following form [38, 39, 46, 47],

$$\boldsymbol{f}_{ij}^{osmotic} = -\frac{k_B T}{2\Omega}\ln\left(\frac{c_\infty}{c_0}\right)\boldsymbol{b}_{ij}\times\boldsymbol{l}_{ij}, \tag{8}$$

where $\boldsymbol{b}_{ij}$ is the Burgers vector of the dislocation segment, and c_∞ is the average vacancy concentration in the sample.

The antiphase boundary (APB) back-driving force is implemented as,

$$\boldsymbol{f}_{ij}^{APB} = \begin{cases} \frac{1}{2}\,\chi^{APB}\,\|\boldsymbol{l}_{ij}\|\sin\left(\frac{\pi}{2}\cdot\frac{L-d}{L}\right)\boldsymbol{n}^s & d \le L \\ 0 & d > L \end{cases} \tag{9}$$

where χ^{APB} is the APB energy per unit area, d is the minimum distance from the segment center to the precipitate surface, L is a transition length over which the APB back-driving force per unit length decays from χ^{APB} to zero, and $\boldsymbol{n}^s$ is the outward normal of the cuboidal precipitate

surface pointing to the segment center. For the calculations of the minimum distance d and the outward surface normal $\boldsymbol{n}^s$, the surface areas at cube edges and corners are approximated as one quarter of a cylinder and one eighth of a sphere respectively, whose radii are both set to be the same as the transition length L. Similar APB back-driving force models have been applied in the DDD simulations of dislocation–precipitate interactions at low and intermediate temperatures, where only dislocation glide is considered, and the direction of the APB back-driving force can be simply set to the opposite direction of dislocation glide [48–52]. In this work, we consider both dislocation glide and climb, and the back-driving force direction is aligned with the outward-pointing surface normal, which efficiently prevents dislocations from entering the precipitate, but allows tangential dislocation motion along the interface.

The force exerted by the misfit stress is calculated using the Peach-Koehler equation:

$$\boldsymbol{f}_{ij}^{misfit} = \frac{1}{2}\,\boldsymbol{\sigma}^{misfit} \cdot \boldsymbol{b}_{ij} \times \boldsymbol{l}_{ij}. \tag{10}$$

The misfit stress is caused by the lattice mismatch between the γ and γ' phases in the nickel-based superalloys, which has been extensively investigated in the past using Finite Element (FE) calculations [3–5, 7, 53–57]. These FE calculation results show that the negative lattice misfit produces biaxial compressive stresses in the matrix, which are parallel to the interfaces and rather uniform in each of the matrix channels. Accordingly, the following misfit stress tensors $\boldsymbol{\sigma}^{misfit}$ are considered in the model for the matrix channels normal to X, Y, and Z directions, respectively,

$$\begin{array}{ccc} \text{channels } (\perp X) & \text{channels } (\perp Y) & \text{channels } (\perp Z) \\ \begin{pmatrix} & & \\ & \sigma^m & \\ & & \sigma^m \end{pmatrix} & \begin{pmatrix} \sigma^m & & \\ & & \\ & & \sigma^m \end{pmatrix} & \begin{pmatrix} \sigma^m & & \\ & \sigma^m & \\ & & \end{pmatrix} \end{array}, \tag{11}$$

where σ^m denotes the misfit stress components. A similar implementation of the misfit stress has been previously used in the DDD simulations of Huang et al. [52].

3 Results

The interfacial dislocation motion and interactions are simulated by applying a tensile stress of $137\,\text{MPa}$ along the $[0\,0\,1]$ direction. For simplicity, isotropic elasticity is adopted with a shear modulus μ of $44.22\,\text{GPa}$ and a Poisson ratio ν of 0.37. The dislocation glide drag coefficient B_g is set to be one percent of the dislocation climb drag coefficient B_c, $B_g = \frac{1}{100}B_c$, to reflect that glide is substantially faster than climb. Similar to the level set dislocation dynamics simulations of Quek et al. [45], the simulation time in this work is normalized by B_c/μ, the quotient of the dislocation climb drag coefficient and the shear modulus, so that the actual value of dislocation climb drag coefficient is not required for the simulation. In the simulated γ/γ' microstructure, the edge length of the cuboidal γ' particles is $1600\,b$, and the width of the γ channels is $400\,b$. The magnitude of the Burgers vector b is $0.25\,\text{nm}$. The APB energy χ^{APB} in the γ' precipitates is set to be $125\,\text{mJ}\,\text{m}^{-2}$ based on the ab initio simulation result of Yashiro et al. [50]. The misfit stress component σ^m in the matrix γ channels is set to be $-100\,\text{MPa}$ based on the FE calculations by

Zhang et al. [7]. The vacancies generated by dislocation climb under the tensile stress are largely adsorbed through porosity growth in the superalloys [10]. The average vacancy concentration in the sample is assumed to be at the equilibrium value, i.e. $c_\infty = c_0$, and the osmotic force defined in Eq. (8) is thus zero in all the simulations. The effect of vacancy supersaturation will be investigated in the future work.

The simulation results can be generally divided into two groups according to the initial configurations: widely-separated interfacial dislocations with the same line sense on the same side of the horizontal channels, and closely-spaced interfacial dislocations with opposite line senses on opposite sides of the horizontal channels. The interfacial dislocations are initially all on the horizontal interfaces is based on the fact that the superposition of external and misfit stresses favors the slip deposition in the horizontal channels. The simulation results for different initial configurations are presented by two means: simulation snapshots showing the actual sequence of dislocation motion and interactions, and line diagrams presenting the corresponding plastic strain accumulation and dislocation density evolution with time.

3.1 Interfacial motion of widely-separated dislocations

The simulations with widely-separated dislocations are designed to investigate interfacial dislocation motion in the absence of considerable internal stresses, where dislocation movement is dominated by the external stress, misfit stress, and line tension of the dislocation. $1/2\,[0\,1\,1]$ interfacial dislocations of mixed and edge characters are considered, and their initial configurations are shown in Fig. 1. Mixed interfacial dislocations are generated by the glide of grown-in $1/2\,\langle 0\,1\,1\rangle\{1\,1\,\bar{1}\}$ dislocations in the horizontal channels, and their line direction is along the intersection line of the glide plane and the γ/γ' interface normal to the $[0\,0\,1]$ direction. Edge interfacial dislocations are formed by interfacial dislocation reactions as will be discussed later. Such edge dislocations are also the basic dislocation configuration considered in various models to interpret high-temperature low-stress creep in single-crystal superalloys [10, 18, 19, 58].

Figure 2 shows the plastic strain accumulation and dislocation density evolution with time in these simulations, which are clearly affected by both the character of the interfacial dislocations and the presence of the misfit stresses.

3.1.1 Mixed dislocations

The simulation of mixed dislocations without considering the misfit stresses is shown in Fig. 3(a). The dislocations initially move along the horizontal interfaces and partially enter the vertical channels (Fig. 3(a), image 1), then become fully trapped in the vertical channels and start to move upwards along the vertical interfaces (Fig. 3(a), image 2), and eventually re-enter the horizontal channels and move again along the horizontal interfaces (Fig. 3(a), image 3). The following snapshots of this simulation record the repetition of these processes, and are thus not shown in the paper. While the dislocations can enter and cross the γ matrix channels simply by glide, the dislocation motion along the γ/γ' interfaces can only be achieved by a combination of glide and climb.

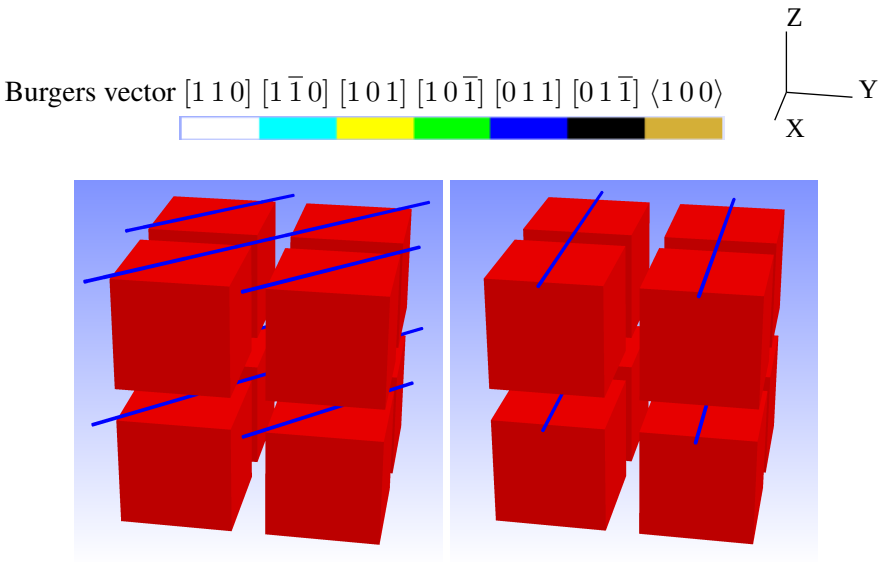

(a) mixed dislocations (b) edge dislocations

Figure 1: Initial configurations of widely-separated dislocations

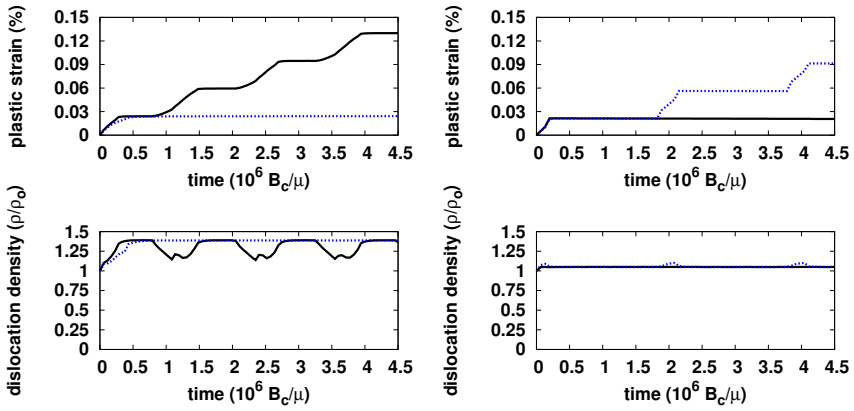

(a) mixed dislocations (b) edge dislocations

Figure 2: Plastic strain accumulation and dislocation density evolution during the interfacial motion of widely-separated dislocations: the simulation considering the misfit stresses is plotted with a dotted blue line (· · ·), and the simulation without considering the misfit stresses is plotted with a solid black line (—).

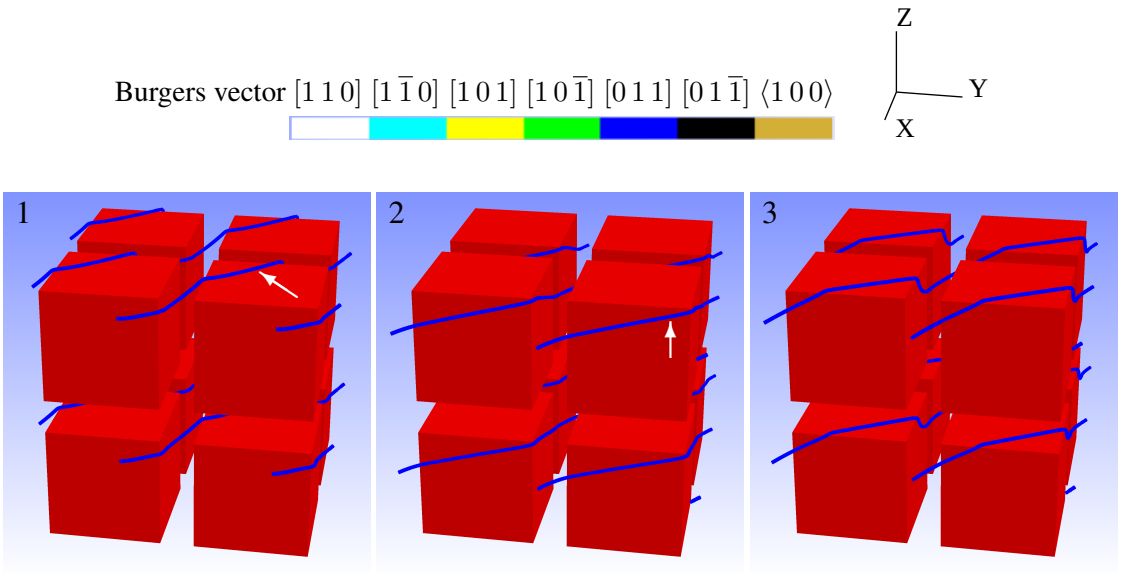

(a) without misfit stresses

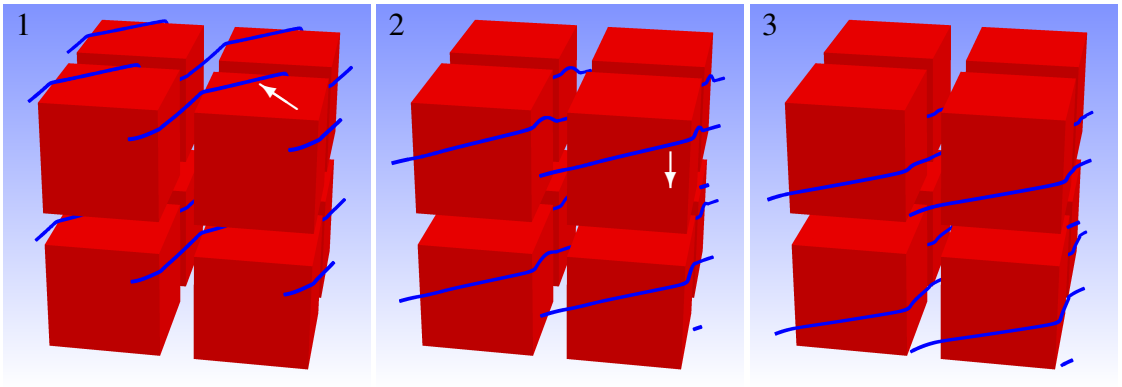

(b) with misfit stresses

Figure 3: Interfacial motion of mixed dislocations

The applied normal stress along the $[0\,0\,1]$ direction generates a Peach-Koehler force in the $(0\,0\,1)$ plane, which activates the dislocation motion along the horizontal interfaces (normal to the $[0\,0\,1]$ direction), but does not affect the dislocation motion along the vertical interfaces (parallel to the $[0\,0\,1]$ direction). Accordingly, the normal plastic strain along the $[0\,0\,1]$ direction is accumulated by the horizontal interfacial motion, but not by the vertical interfacial dislocation motion along the $[0\,0\,1]$ direction. The strain accumulating and non-accumulating periods associated with these processes can be clearly distinguished in the top diagram of Fig. 2(a) (solid black line).

The vertical interfacial dislocation motion is driven by the line tension force that acts to minimize the dislocation core energy. The line tension force is associated with the dislocation configuration trapped in the vertical channels, which gradually reduces as the dislocation moves

out of the vertical channels and changes its line configuration. Such a process is reflected by the dislocation density change in the simulation shown in the bottom diagram of Fig. 2(a) (solid black line).

The simulation of mixed dislocations considering the misfit stresses is shown in Fig. 3(b). It can be seen that in the presence of the misfit stresses, the dislocations move downwards once they are trapped in the vertical channels (Fig. 3(b), images 2 and 3). Note that the simulated dislocations have a $1/2$ $[0\,1\,1]$ Burgers vector, which are not activated by the misfit stress component along the $[1\,0\,0]$ direction. The misfit stress component along the $[0\,0\,1]$ direction does not affect the vertical interfacial dislocation motion. Only the force exerted by the misfit stress component along the $[0\,1\,0]$ direction can overcome the line tension force, and drag the dislocation moving downwards along the vertical channels. This slow dislocation movement along the vertical channels does not contribute to the plastic strain along the $[0\,01]$ direction, and causes no change in the dislocation density, Fig. 2(a) (dotted blue lines).

3.1.2 Edge dislocations

The simulation of edge dislocations without considering the misfit stresses is shown in Fig. 4(a). The dislocations primarily move along the horizontal interfaces towards the edges of the cuboidal γ' precipitates (Fig. 4(a), image 1), later glide across the vertical channels and reach the vertical interfaces of neighboring precipitates (Fig. 4(a), image 2), and lastly move downwards along the vertical interfaces (Fig. 4(a), image 3). The vertical dislocation motion along the $[0\,0\,1]$ direction also results from the line tension force. Due to the different dislocation configurations, the line tension force for the trapped edge dislocation drags it moving downwards along the vertical interfaces (Fig. 4(a), image 2), while the line tension force for the trapped mixed dislocation pulls it moving upwards along the vertical interfaces (Fig. 3(a), image 2). Since the trapped edge dislocation is mostly a straight line, the associated line tension force is low. The vertical dislocation motion is so slow that the dislocations have not reached the edges of the precipitates by the end of the simulation. This slow dislocation movement along the vertical interfaces does not contribute to the plastic strain along the $[0\,01]$ direction, and causes no change in the dislocation density, Fig. 2(b) (solid black lines).

The simulation of edge dislocations considering the misfit stresses is shown in Fig. 4(b). It can be seen that in the presence of the misfit stress, the dislocations have moved a long distance along the vertical interfaces to reach the edges of the precipitates (Fig. 4(b), images 2 and 3). The dislocations will then glide across the horizontal channels and move again on the horizontal interfaces, which is not shown in the paper. The cross-channel glide and horizontal interfacial dislocation motion contribute to the plastic strain along the $[0\,0\,1]$ direction, which is reflected in the plastic strain–time diagram of Fig. 2(b) (dotted blue line).

3.2 Interfacial motion and interactions of closely-spaced dislocations

The simulations with closely-spaced dislocation arrays are intended to reveal the effect of dislocation interactions on interfacial dislocation motion. The initial interfacial dislocation networks are constructed by considering one or two activated $\langle 0\,1\,1\rangle\{1\,1\,\overline{1}\}$ slip systems in the horizontal

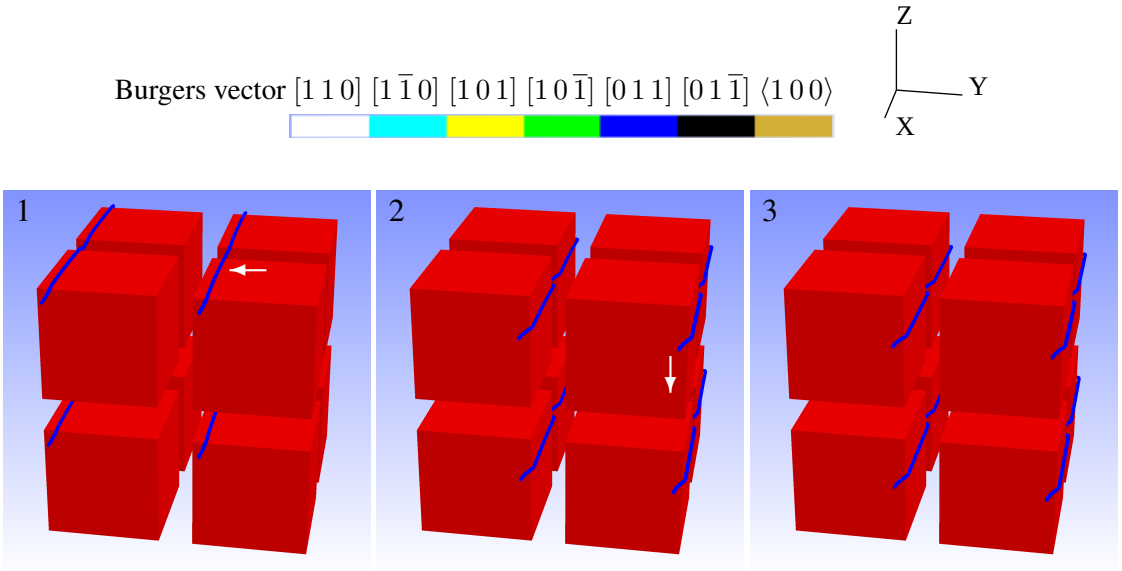

(a) without misfit stresses

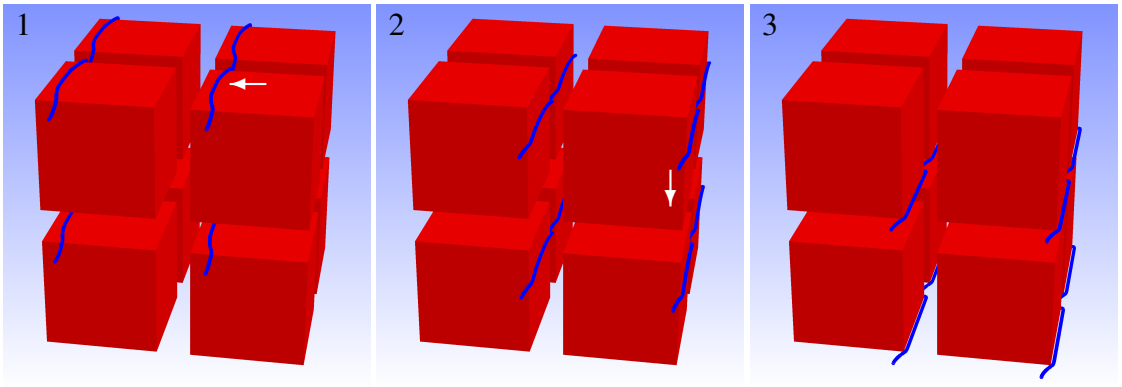

(b) with misfit stresses

Figure 4: Interfacial motion of edge dislocations

channels that deposit mixed dislocations of opposite line senses on opposite interfaces, Fig. 5. The average dislocation spacing in the interfacial dislocation networks is $90\,\mathrm{nm}$. Each group of the interfacial dislocation networks corresponds to a dislocation density of $5 \times 10^{13}\,\mathrm{m}^{-2}$.

Figure 6 shows the plastic strain accumulation and dislocation density evolution with time in these simulations, which are largely affected by the different types of interfacial dislocation interactions. For the simulations starting with the same initial configuration, the plastic strain accumulation and dislocation density evolution also varies when conducted with the misfit stresses (dotted blue line in Fig. 6) and without the misfit stresses (solid black line in Fig. 6).

In terms of the dislocation density evolution, the simulation results can be categorized into three groups. For the simulations of collinear or Lomer junction forming slip systems, the dislocation density starts to decrease at the onset of creep and can drop to zero at the end of the

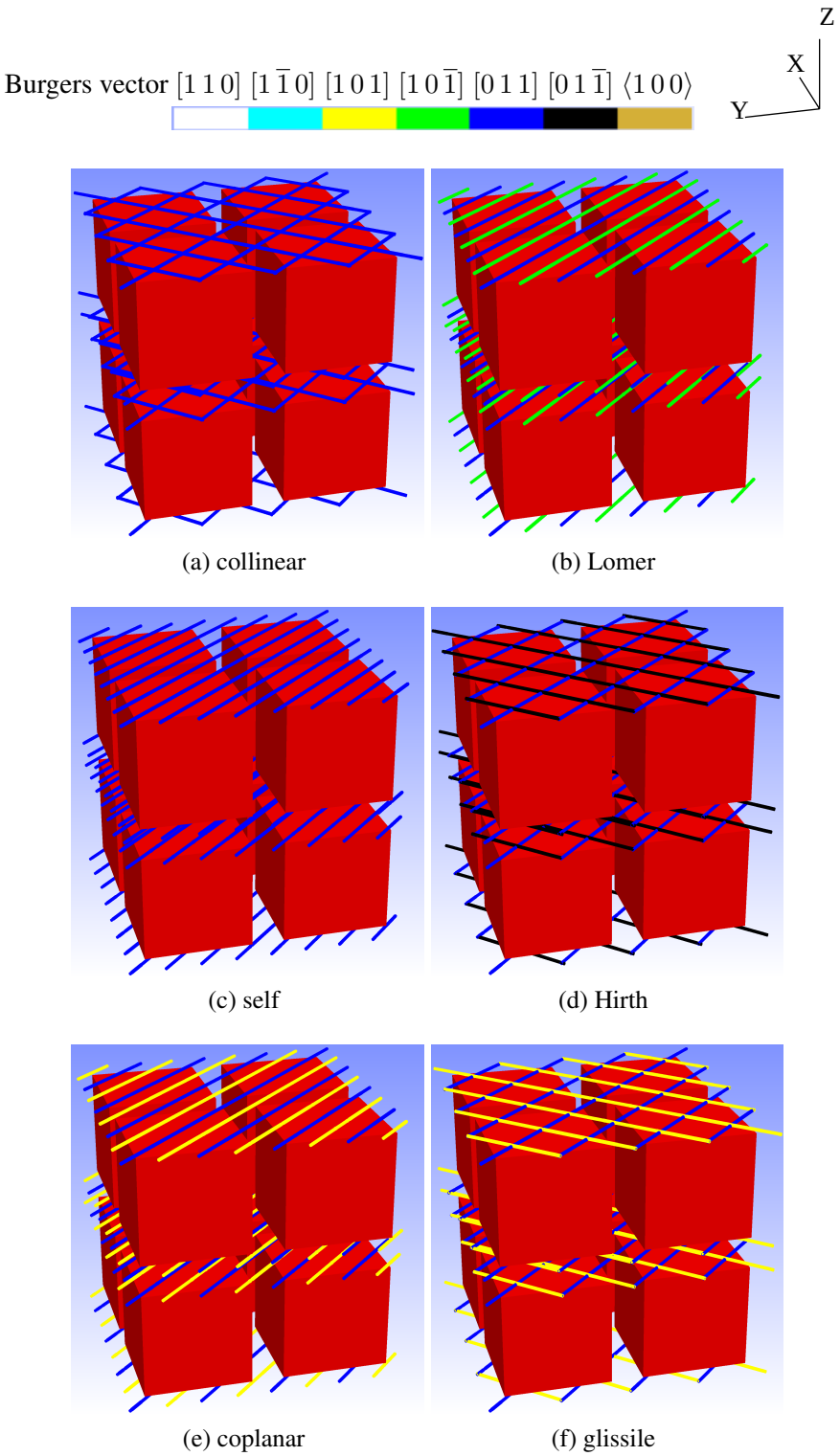

Figure 5: Initial configurations of interfacial dislocation networks involving different types of dislocation interactions

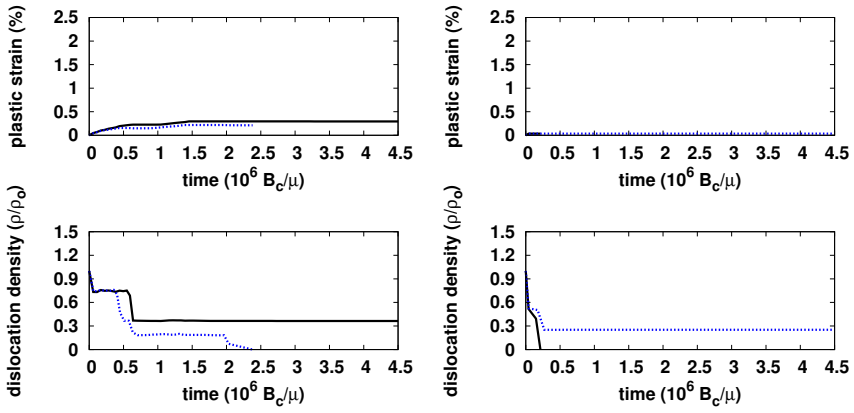

(a) collinear

(b) Lomer

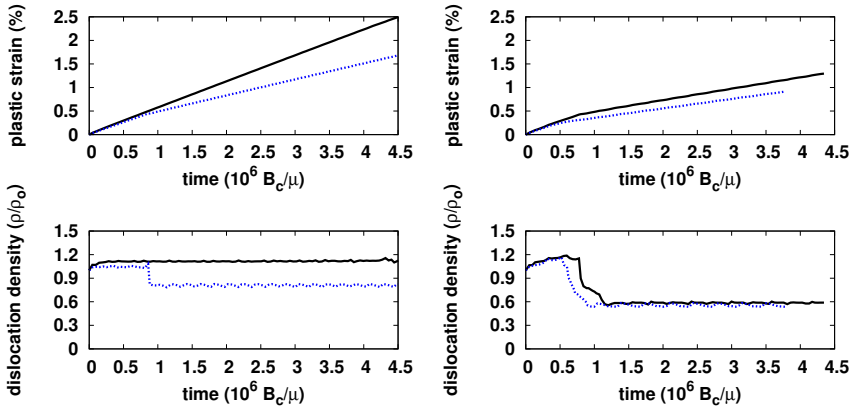

(c) self

(d) Hirth

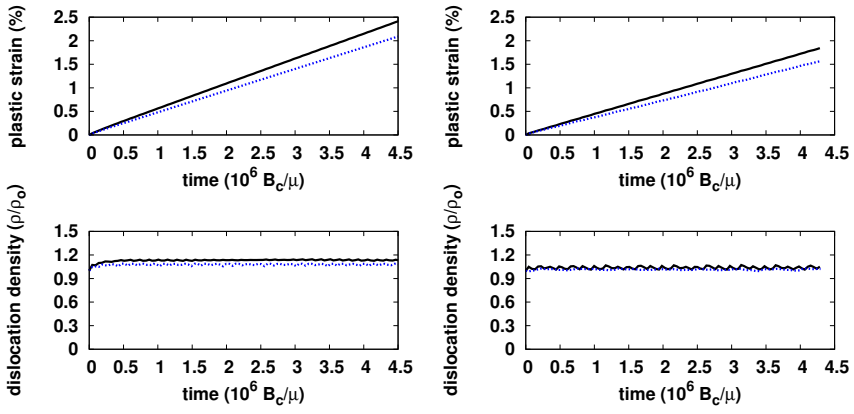

(e) coplanar

(f) glissile

Figure 6: Plastic strain accumulation and dislocation density evolution during the interfacial motion of dislocation networks involving different types of dislocation interactions: the simulation considering the misfit stresses is plotted with a dotted blue line ($\cdots$), and the simulation without considering the misfit stresses is plotted with a solid black line (—).

simulation, Fig. 6(a),(b). For the simulations of single slip system or Hirth junction forming slip systems, a drop in dislocation density occurs during the intermediate stage before it remains constant till the end of the simulation, Fig. 6(c),(d). For the simulations of coplanar or glissile junction forming slip systems, the dislocation density remains almost constant during the simulation, Fig. 6(e),(f).

3.2.1 Collinear slip systems

Figure 7 shows the interfacial dislocation motion and interaction on collinear slip systems under the external and misfit stresses. Comparing Fig. 5(a) and Fig. 7(a), the collinear annihilation of the two dislocation arrays results in an array of dislocations in zig-zag shapes. These dislocations are later straightened due to their line tension, Fig. 7(b), and become straight edge dislocations along the $[1\,0\,0]$ direction, Fig. 7(c). Such edge dislocations are very often observed in creep experiments [7, 16, 57] and are more effective at relieving the misfit stress than the glide-deposited mixed dislocations [13]. It is explicitly shown here that these edge dislocations are formed through the short-range reactions between the glide-deposited mixed dislocations on collinear slip systems.

Similar to the previous simulations, the edge dislocations can enter the vertical channels by glide, and move along the vertical interfaces in a combination of glide and climb. The edge dislocations now at the vertical interfaces have entered the vertical channels from opposite horizontal interfaces and thus have opposite line senses. The antiparallel edge dislocations are moving in opposite directions along the vertical channels, Fig. 7(c). In the meantime, more edge dislocations are entering the vertical channels, Fig. 7(d). The dislocations entering from the bottom interfaces are moving up along the vertical interfaces to meet the dislocations moving on the top interfaces at the precipitate corners, Fig. 7(e). The antiparallel dislocations annihilate partially and form rectangular dislocation loops, Fig. 7(f), which shrink at the edges of the precipitates, Fig. 7(g), and eventually disappear, Fig. 7(h).

The remaining dislocations are all moving along the interfaces in the vertical channels, where the misfit stress component along the $[0\,0\,1]$ direction partially cancels the external stress. The mutual attraction of the antiparallel dislocations on opposite interfaces can overcome the remaining external stress, and lead to the annihilation of a pair of dislocations in the vertical channels, Fig. 7(h),(i). The mutual repulsion of dislocations of the same sign on the same interface pushes another pair of dislocations out of the vertical channels, which are then moving along the horizontal interfaces, Fig. 7(i). The following snapshots of this simulation are not shown here. These dislocations will move to the opposite edges of the horizontal interfaces, re-enter the vertical channels, and annihilate each other. The dislocation density drops to zero after this last annihilation, which can be seen in the dislocation density–time diagram in Fig. 6(a) (dotted blue line).

The simulation of the collinear interfacial dislocation motion and interactions in the absence of the misfit stresses is not shown here. The main difference is that the annihilation across the vertical channels in the presence of the misfit stress shown in Fig. 7(h),(i) does not occur in the absence of the misfit stress. In the latter case, a constant dislocation density is maintained till the end of the simulation, which is recorded in the dislocation density–time diagram in Fig. 6(a)

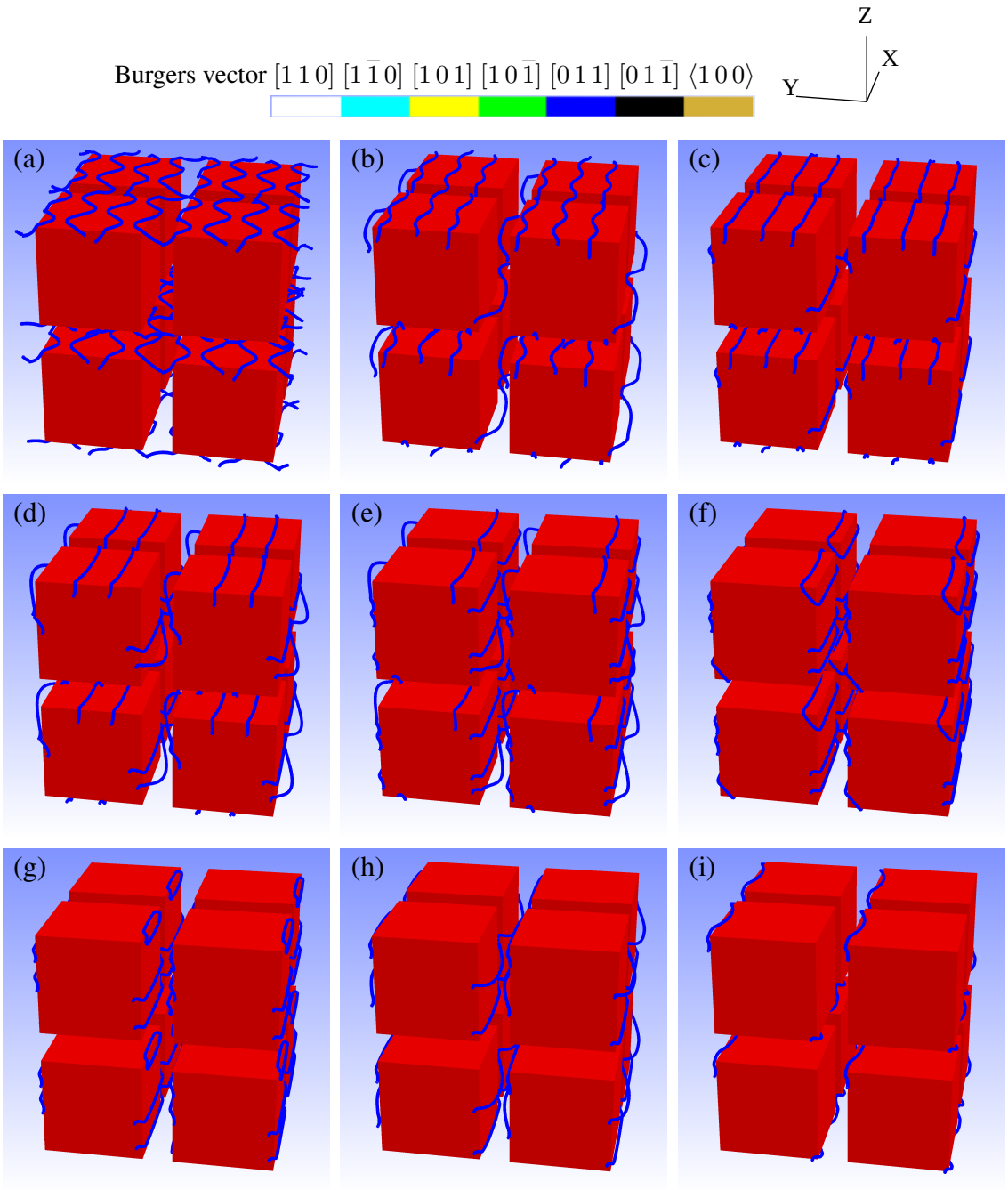

Figure 7: Interfacial dislocation motion and interaction on collinear slip systems

(solid black line).

3.2.2 Lomer junction forming slip systems

Figure 8 shows the interfacial dislocation motion and interaction on Lomer junction forming slip systems under the external stress. The intersection lines of these two slip planes and the γ/γ' horizontal interfaces are along the same line direction, and the initial network consists of parallel dislocations, Fig. 5(b). The dislocations are mainly moving along the horizontal interfaces in a combination of glide and climb, and partially squeezed into the vertical channels by glide, Fig. 8(a). The $1/2\ [0\,1\,1]$ and $1/2\ [1\,0\,\bar{1}]$ dislocations attract each other and merge to $1/2\ [1\,1\,0]$ junctions first at the vertical channels, where they are closer to each other, Fig. 8(b). The junction zipping completes as the parent $1/2\ [0\,1\,1]$ and $1/2\ [1\,0\,\bar{1}]$ dislocations approach each other on the horizontal interfaces, Fig. 8(c). The newly formed $1/2\ [1\,1\,0]$ dislocations are not activated by the external stress along the $[0\,0\,1]$ direction. The dislocations of opposite signs on opposite interfaces move towards each other due to their mutual attraction, Fig. 8(d).

The junction dislocations inherit the curved line configurations of their parent dislocations that were partially squeezed in the vertical channels. As the dipolar dislocations approach each other, some parts of the dislocations are directly annihilated, and the remaining parts of the dislocations form dislocation loops, Fig. 8(e),(f). Depending on the curvatures of the junction dislocations, the loops formed due to the partial annihilation of junction dislocations are of different sizes. The break-up of dislocation dipoles into prismatic loops has been frequently observed in high temperature deformation or subsequent annealing [59–62]. In our case, each loop formed is not entirely prismatic, but a mixture of glide and prismatic loops. The loops shrink by both glide and climb. As dislocations glide faster than they climb, the glide parts of the loops shrink first, which transforms the mixed loops into prismatic loops. During these processes, the loop shrinkage is accompanied by the rotation of the dislocation loop plane, Fig. 8(g),(h). Eventually all the dislocations are annihilated, as the loops self-annihilate by areal shrinking, Fig. 8(i).

The simulation of the Lomer junction forming slip systems considering the misfit stresses is not shown. The main difference is that the annihilation of the $1/2\ [1\,1\,0]$ junction dislocations are partially prevented in the presence of the misfit stress. The remaining dipolar dislocations are far away from each other, and separated by the misfit stress on opposite horizontal interfaces. The dislocation density–time diagram in Fig. 6(b) records the partial annihilation in the presence of the misfit stress (dotted blue line) and the full annihilation in the absence of the misfit stress (solid black line).

3.2.3 Single slip system

Figure 9 shows the interfacial dislocation motion and self-interaction on a single slip system under the external and misfit stresses. The initial configuration consists of dipolar arrays of mixed dislocation on opposite horizontal interfaces, Fig. 5(c). Probst-Hein et al. [5] have conducted static dislocation calculations of such dislocation networks to evaluate the Peach-Koehler (PK) forces on the network dislocations as a function of the number of dislocations in the network. As the number of network dislocations increases (the network dislocation spacing decreases), the

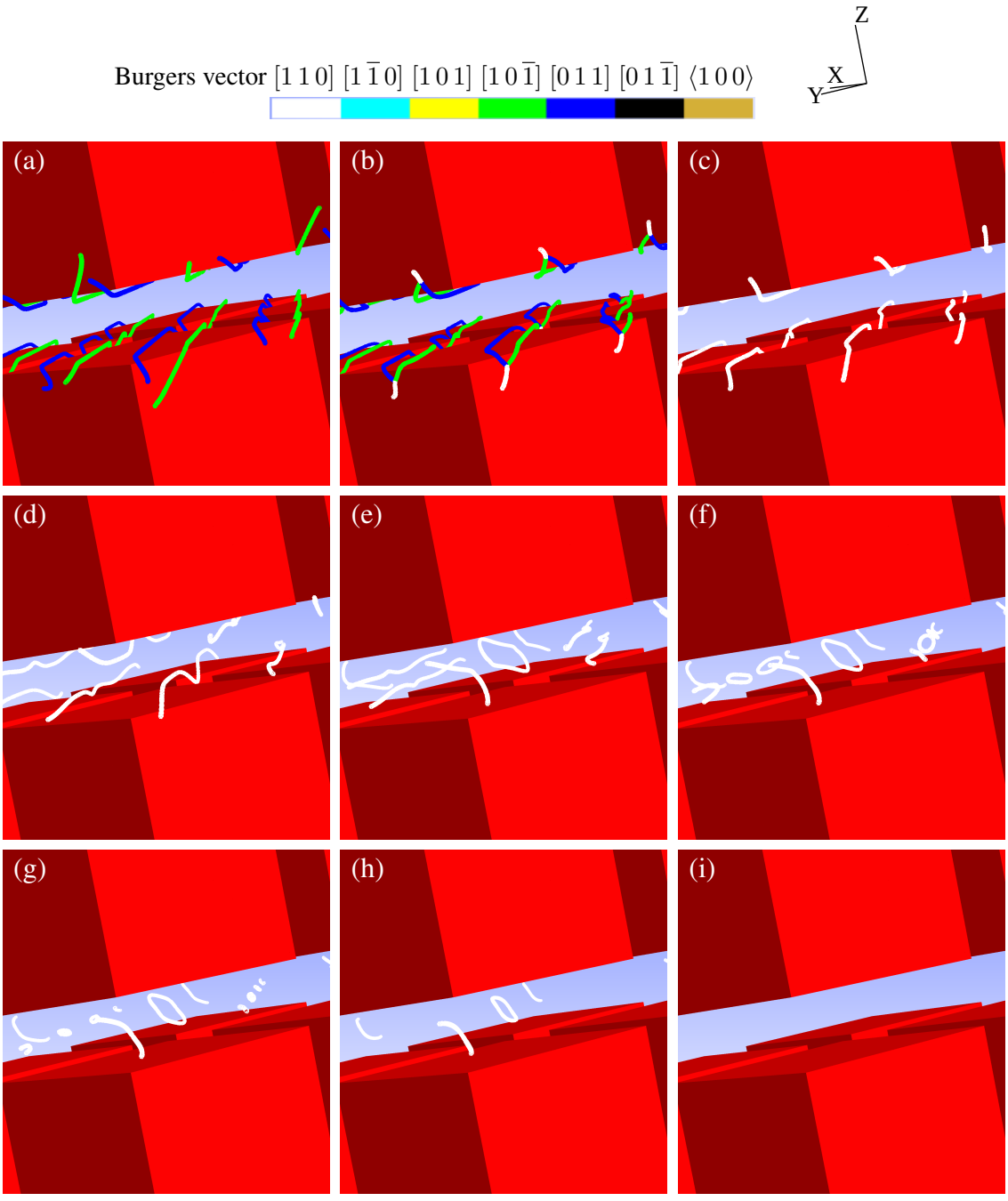

Figure 8: Interfacial dislocation motion and interaction on Lomer junction forming slip systems

dislocation internal stresses eventually overcome the external and misfit stresses, which causes the sign change of the PK forces. Our dislocation dynamics simulation shows that due to the trapping of dislocations at the vertical channels, the local dislocation spacing there becomes smaller than the average dislocation spacing, Fig. 9(a),(b). When the internal stresses exceed the external stress at the channel crosses, the dipolar dislocations there move towards each other and annihilate, Fig. 9(c). The annihilation is similar to the Lomer junction annihilation, which consists of two general steps, i.e. partial annihilation leads first to loop formation, Fig. 9(d), and these loops self-annihilate by areal shrinking, Fig. 9(e),(f). Due to the simulation view presented here, only halves of the dislocation loops can be seen. After this annihilation, the internal stresses are reduced and no longer high enough to overcome the external stress. A constant dislocation density is then maintained till the end of the simulation, Fig. 6(c) (dotted blue line in the dislocation density–time diagram).

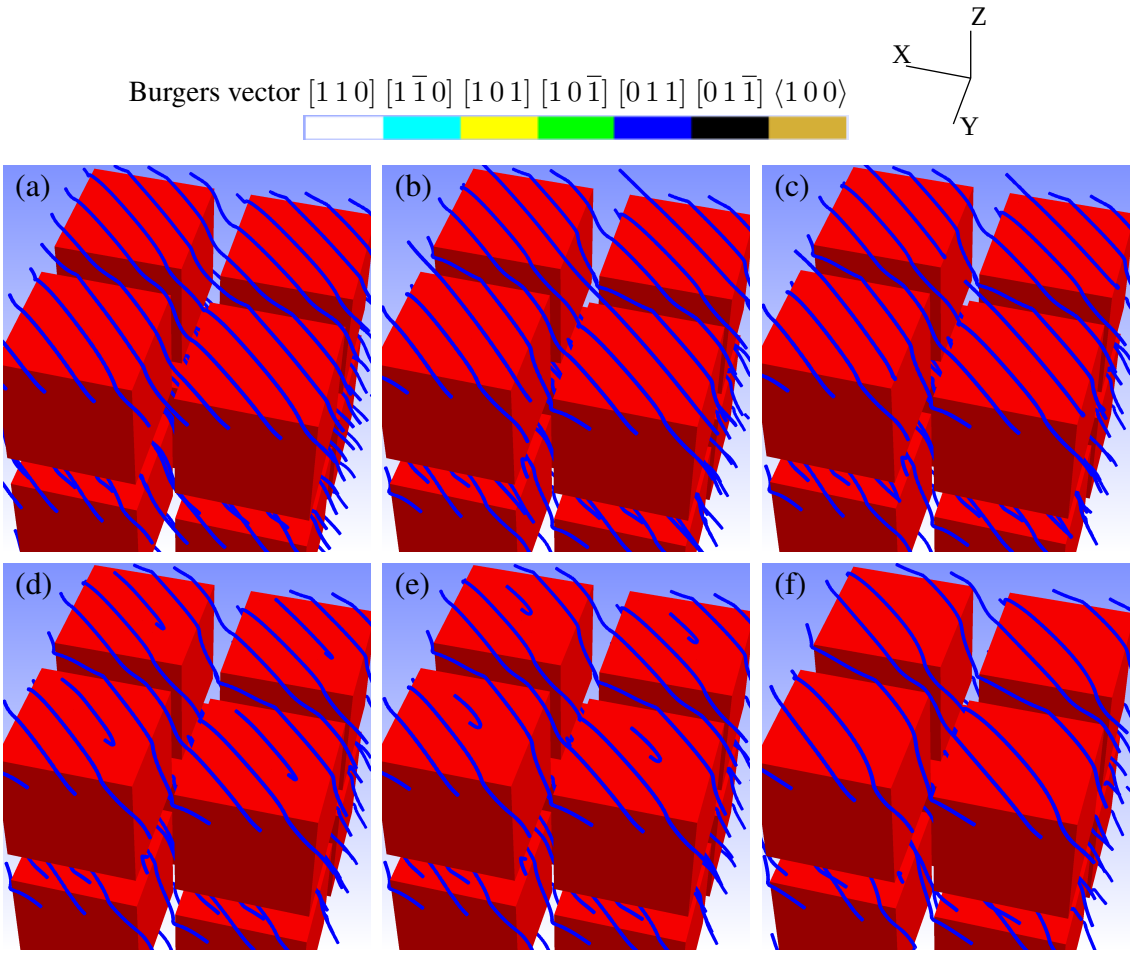

Figure 9: Interfacial dislocation motion and self-interaction on a single slip system

The interfacial dislocation motion and self-interaction in the absence of the misfit stresses is not shown. As observed in Fig. 3, without the inward dragging caused by the misfit stress, the mixed dislocations can easily move out of the vertical channels due to the outward pulling by the

line tension force. The local dislocation spacing decrease and dipole annihilation in the presence of the misfit stress shown in Fig. 9(e),(f) does not occur in the absence of the misfit stress. The dislocation network structure then hardly changes, and the dislocation density is almost constant during the simulation, Fig. 6(c) (solid black line in the dislocation density–time diagram).

3.2.4 Hirth junction forming slip systems

Figure 10 shows the interfacial dislocation motion and interaction on Hirth junction forming slip systems under the external and misfit stresses. The initial configuration consists of dipolar square dislocation networks on opposite horizontal interfaces, Fig. 5(d). The $60°$ $1/2$ $[0\,1\,1]$ and $1/2$ $[0\,1\,\bar{1}]$ dislocations in the same network are repulsive against each other, and do not form Hirth junctions, Fig. 10(a). As they move to the vertical channels, their mutual repulsion pushes the $1/2$ $[0\,1\,\bar{1}]$ dislocations out of the vertical channels, and the $1/2$ $[0\,1\,1]$ towards the center of the vertical channels, Fig. 10(b),(c). The dislocations that entered the vertical channels from the bottom interfaces are moving up along the vertical interfaces to meet the dislocations moving on the top interfaces at the precipitate corners, Fig. 10(d). Portions of the dislocations are annihilated in the vertical channels normal to the $[1\,0\,0]$ direction, which leaves irregular dislocation loops at the precipitate corners and in the vertical channels normal to the $[0\,1\,0]$ direction, Fig. 10(e). The triangle parts of the dislocation loops shrink and disappear first at the precipitate corners, and the remaining debris of the dislocation loops continue to shrink in the vertical channels normal to the $[0\,1\,0]$ direction, Fig. 10(f). In the meantime, the $1/2$ $[0\,1\,\bar{1}]$ dislocations enter the vertical channels, and partially merge with the shrinking $1/2$ $[0\,1\,1]$ dislocation loops to form $[0\,1\,0]$ Hirth junctions, Fig. 10(g). As the $1/2$ $[0\,1\,1]$ dislocation loops shrink to disappear, the $[0\,1\,0]$ Hirth junctions are later unzipped, Fig. 10(h),(i).

The simulation of the Hirth junction forming slip system without considering the misfit stresses is not shown. In the absence of the misfit stress, the mutual repulsion of $1/2$ $[0\,1\,1]$ and $1/2$ $[0\,1\,\bar{1}]$ dislocations still leads to the separation of the dislocation networks and to the complete annihilation of the $1/2$ $[0\,1\,1]$ dislocations. However, the movement of the $1/2$ $[0\,1\,1]$ dislocations along the vertical channels becomes slow, and the corner encounter of antiparallel dislocations in the presence of the misfit stress shown in Fig. 10(d),(e) does not occur in the absence of the misfit stress. The annihilation starts at the channel crosses, which leaves dislocation loops shrinking to disappear in the vertical channels. The delayed annihilation due to the absence of the misfit stress can be seen in the dislocation density–time diagram of Fig. 6(d)

3.2.5 Coplanar slip systems

The interfacial dislocation motion and interaction on coplanar slip systems is shown in Fig. 11(a) for the simulation in the absence of the misfit stresses, and in Fig. 11(b) for the simulation in the presence of the misfit stresses. The initial configuration consists of dipolar arrays of parallel dislocations on opposite horizontal interfaces, Fig. 5(e), similar to the Lomer junction and self-interaction cases, Fig. 5(b),(c). During the whole simulations, the coplanar interfacial dislocations move through the γ/γ' structures in a steady state, Fig. 11. Unlike the Lomer junction case, the mixed dislocations of different Burgers vectors on the coplanar slip systems are repulsive

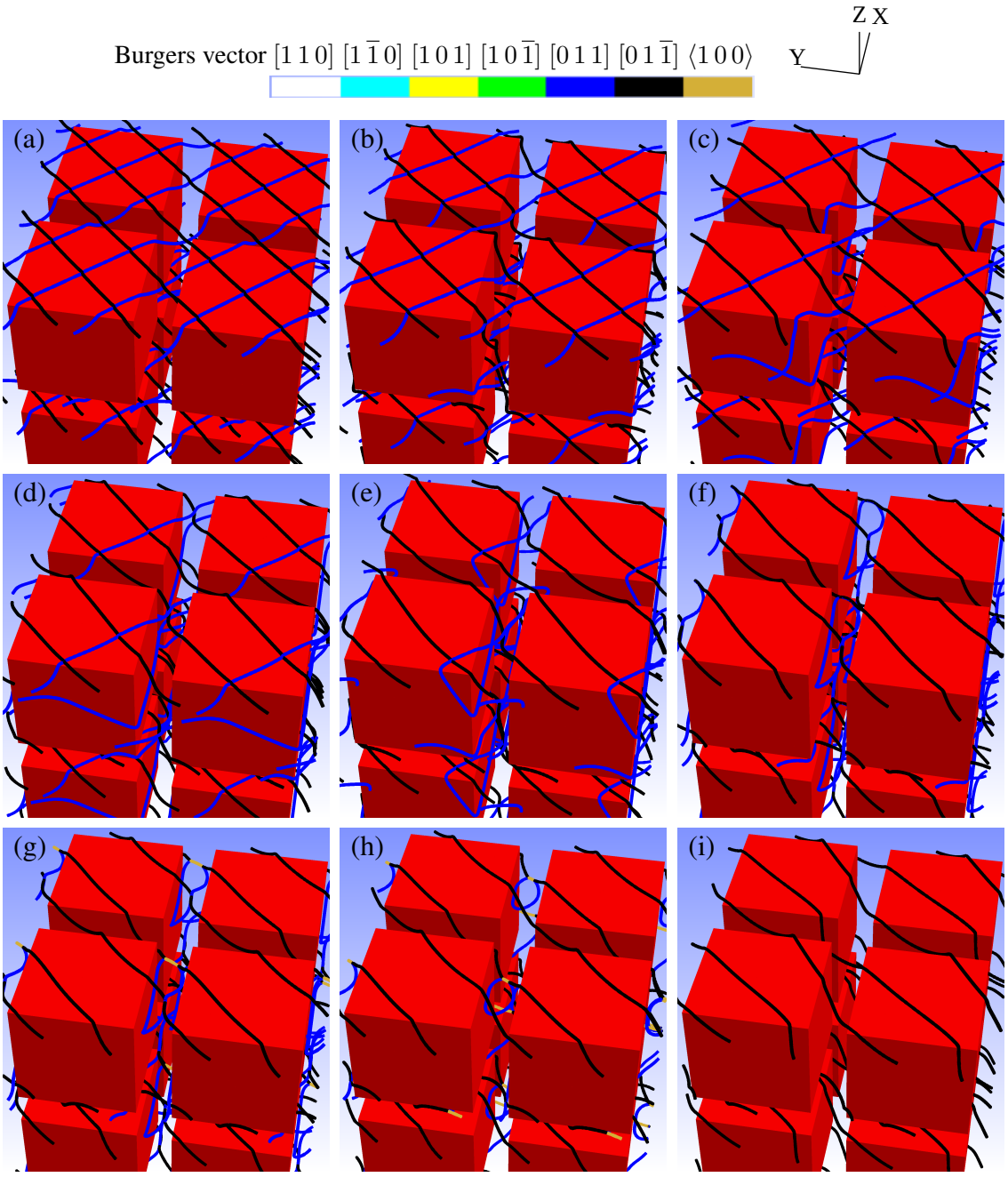

Figure 10: Interfacial dislocation motion and interaction on Hirth junction forming slip systems

against each other, and do not merge to form dislocation junctions. Unlike the self-interaction case, dislocation annihilation does not occur on the coplanar slip systems even in the presence of the misfit stress. The dislocation trapping at the vertical interfaces due to the misfit stress can be seen by comparing Fig. 11(a) and Fig. 11(b). The $1/2\ [0\,1\,1]$ dislocations are trapped in the vertical channels normal to the $[1\,0\,0]$ direction (due to the $[0\,1\,0]$ misfit stress component), and $1/2\ [1\,0\,1]$ dislocations are trapped in the vertical channels normal to the $[0\,1\,0]$ direction (due to the $[1\,0\,0]$ misfit stress component). The dislocation density is almost constant during both simulations, but the strain rate is lower in the presence of the misfit stress, Fig. 6(e).

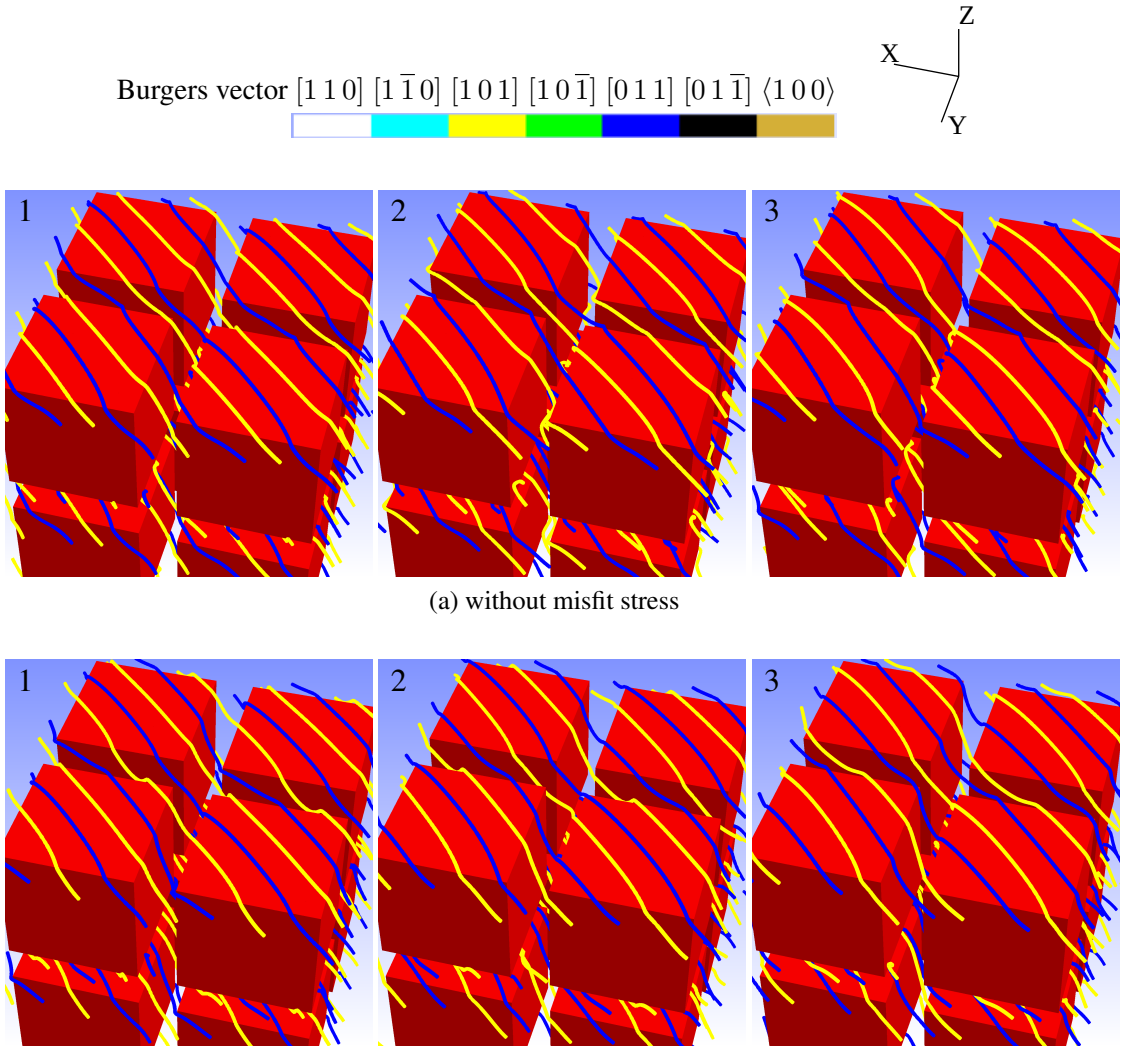

(a) without misfit stress

(b) with misfit stress

Figure 11: Interfacial dislocation motion and interaction on coplanar slip systems

3.2.6 Glissile junction forming slip systems

Figure 12 shows the interfacial dislocation motion and interaction on glissile junction forming slip systems under the external and misfit stresses. The initial configuration consists of dipolar square dislocation networks on opposite horizontal interfaces, Fig. 5(f), similar to the collinear and Hirth junction cases, Fig. 5(a),(d). The $60°$ $1/2\,[0\,1\,1]$ and $1/2\,[1\,0\,1]$ dislocations in the same network react and form $1/2\,[1\,\bar{1}\,0]$ junctions at their intersections, Fig. 12(a). As the junction zipping continues, the square dislocation networks are transformed into hexagonal dislocation networks, Fig. 12(b).

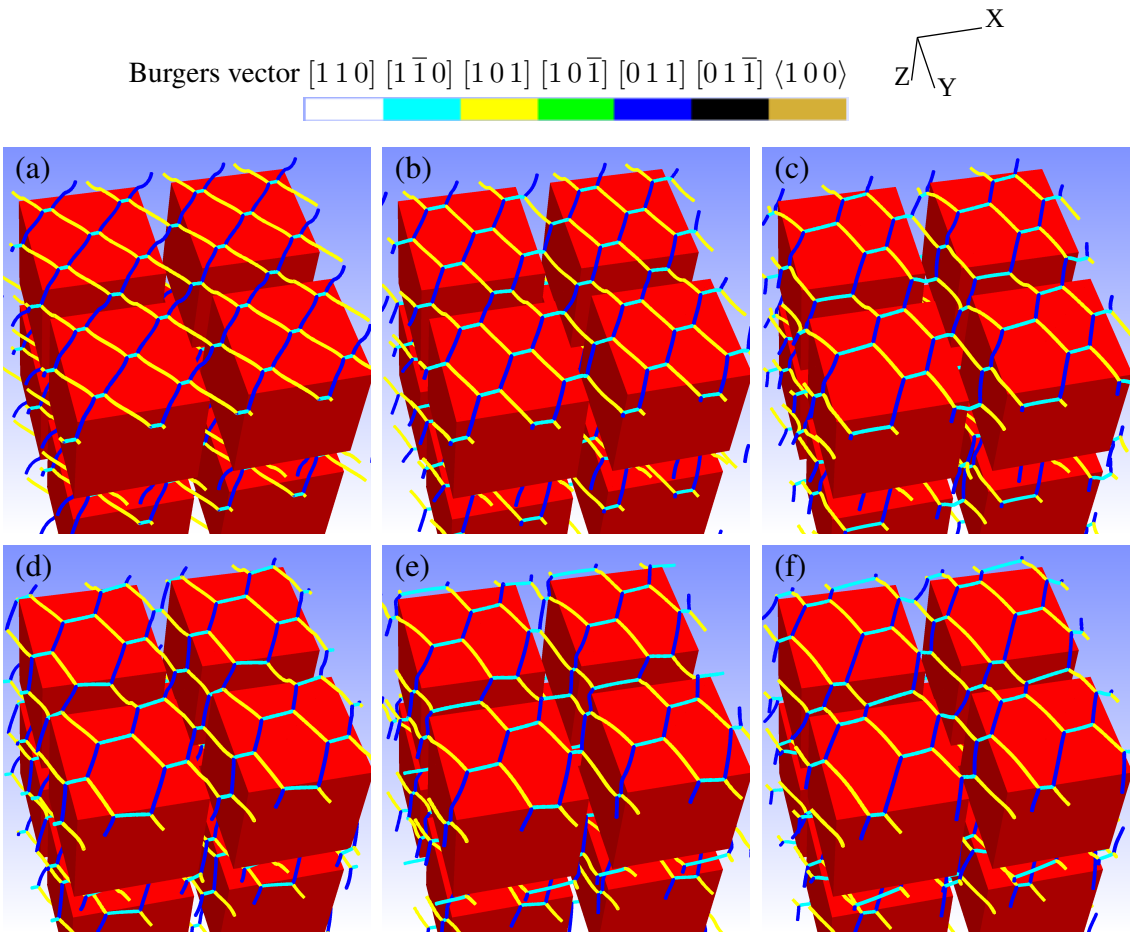

Figure 12: Interfacial dislocation motion and interaction on glissile junction forming slip systems

The $1/2\,[1\,\bar{1}\,0]$ junction dislocations are formed approximately along the $[1\,0\,0]$ direction, which are not activated by the normal stress components along the $[0\,0\,1]$ and $[1\,0\,0]$ directions. The junction dislocations are driven by the misfit stress component along the $[0\,1\,0]$ direction to move along the $[0\,0\,1]$ directions, but do not move in the horizontal $(0\,0\,1)$ plane. The horizontal motion of the hexagonal dislocation networks proceeds via the interfacial dislocation motion of the $1/2\,[0\,1\,1]$ and $1/2\,[1\,0\,1]$ parent dislocations, and involves junction zipping by the lead-

ing parent dislocations and junction unzipping by the tailing parent dislocations. The junction lengths increase when the tailing parent dislocations are trapped at the vertical interfaces, and decrease when the leading parent dislocations are trapped at the vertical interfaces, Fig. 12(c). As the parent dislocations move out of the vertical channels, the junction dislocations tend to resume their original length, Fig. 12(d). As more network dislocations pass through the vertical channels, the mesh of the hexagonal dislocation networks become irregular, Fig. 12(e),(f).

The simulation of the glissile junction forming slip system without considering the misfit stresses is not shown. The main difference is that the mesh of the hexagonal dislocation networks becomes less irregular in the absence of the misfit stress than those in the presence of the misfit stress as shown in Fig. 12(e),(f), The dislocation density is almost constant during both simulations, but the strain rate is lower in the presence of the misfit stress, Fig. 6(f).

4 Discussion

The simulation results show that interfacial dislocation motion and dynamic recovery in single-crystal superalloys can be strongly altered by interfacial dislocation interactions. Collinear annihilation transforms the square dislocation networks into parallel arrays of edge dislocations, which move freely along the horizontal and vertical interfaces, and annihilate each other at the precipitate corners. Lomer junction formation leaves long inactivated dislocation dipoles on opposite horizontal interfaces, which break up into dislocation loops that self-annihilate by areal shrinking. The interfacial dislocation motion on coplanar and glissile junction forming slip systems proceeds steadily, and does not lead to dynamic recovery at all.

Although these simulations of interfacial dislocation motion and interactions are essential to understand plastic deformation during high temperature creep, the plastic strain–time curves obtained from these simulations should not be directly interpreted as creep curves. Several processes that could contribute or affect the creep strain accumulation are not considered in the model, which include the regeneration of interfacial dislocation networks after recovery, directional coarsening (rafting) of the γ' precipitates, and $\langle 1\,0\,0\rangle$ dislocations cutting of the rafted γ' precipitates. We shall discuss the potential effect of these processes on high temperature creep based on the present simulation results.

The recovery of the interfacial dislocation networks relieves the internal back stress, and the grown-in dislocations could again glide in the horizontal channels and form new interfacial dislocation networks. The softening effect of dynamic recovery is evident, as the glide of the grown-in dislocations proceeds much faster than the interfacial dislocation motion in a combination of glide and climb.

During high temperature creep of single-crystal superalloys, the tensile stress along the $[0\,0\,1]$ direction would ideally activate eight $\langle 0\,1\,1\rangle\{1\,1\,\bar{1}\}$ slip systems simultaneously, but in reality the slip systems are gradually activated in a random sequence [13–15]. Depending on the activated slip system, dynamic recovery and creep softening may initialize rapidly (collinear and Lomer junction forming slip systems) or not occur at all (coplanar and glissile junction forming slip systems), which can lead a strong scatter of creep curves at the early stage of high temperature creep.

The dynamic recovery on the single slip system and Hirth junction forming slip systems does not occur initially but at a plastic strain up to 0.5%. This is also the strain regime where substantial rafting takes place, re-shaping the originally cuboidal morphology of the γ' precipitates into a lamellar-type arrangement perpendicular to the $[0\,0\,1]$ loading axis [6, 12, 15, 56, 63]. Once the rafting has profoundly changed the shape of the precipitates into such a lamellar morphology, dynamic recovery associated with the vertical interfacial motion will no longer occur. The hardening effect of rafting shall be expected due to the prevention of further dynamic recovery in the vertical channels.

Dynamic recovery and creep deformation in the rafted γ/γ' microstructures are mainly related to $\langle 1\,0\,0\rangle$ dislocations cutting of the γ' precipitates [12]. There are several mechanisms proposed in the literature on the $\langle 1\,0\,0\rangle$ dislocation formation in the single-crystal superalloys [11, 12, 57, 58, 64]. One of the mechanisms is that the $\langle 1\,0\,0\rangle$ dislocations are formed as Hirth junctions [11, 12, 57]. Our simulation result shows that the Hirth junctions are not formed directly by the glide-deposited 60° dislocations, but at the later stage of high temperature creep when the glide-deposited dislocations have gone through a large line-orientation change during the interfacial dislocation motion and interaction.

5 Summary

We simulated interfacial motion of mixed dislocations, edge dislocations and different types of dislocation networks in the channel structures of single-crystal superalloys.

For widely-separated dislocations, the horizontal interfacial dislocation motion is mainly driven by the external stress, and the vertical interfacial dislocation motion is largely affected by the presence of the misfit stress. The line tension force, depending on the trapped dislocation configuration, can drive mixed and edge dislocations to move in opposite directions along the vertical interfaces.

For dipolar dislocation networks, the interfacial dislocation motion and dynamic recovery is dominated by interfacial dislocation interactions. The short-range reactions of collinear annihilation and Lomer junction formation lead to recovery at the early stage of high temperature creep. The misfit stress induces and accelerates the dynamic recovery on the single slip system and Hirth junction forming slip systems, but slows down the steady interfacial dislocation motion on the coplanar and glissile junction forming slip systems.

It is found that $1/2\,\langle 0\,1\,1\rangle$ edge dislocations along the $\langle 1\,0\,0\rangle$ directions are formed by glide-deposited mixed dislocations on collinear slip systems. Such a finding provides a theoretical basis for creep models built on such dislocation configurations, but at the same time suggests the incapability of these models to describe interfacial dislocation motion on slip systems involving other types of dislocation interactions.

The simulation of Hirth junction forming slip systems supports the theoretical assumption that the $\langle 1\,0\,0\rangle$ dislocations are formed as Hirth junctions. However, the Hirth junctions are only formed when the glide-deposited dislocations have gone through a large line-orientation change during the interfacial dislocation motion and interaction, which indicates that the $\langle 1\,0\,0\rangle$ dislocation formation and associated recovery process of $\langle 1\,0\,0\rangle$ dislocation cutting does not

occur at the early stage of high temperature creep.

Acknowledgments

We thank Ricardo Lebensohn for his continuous support and Michael Demkowicz for helpful discussions. This work was performed under the auspices of the U.S. Department of Energy by Lawrence Livermore National Laboratory under Contract DE-AC52-07NA27344.

References

[1] Rae C.M.F. and Reed R.C., 2007. Primary creep in single crystal superalloys: Origins, mechanisms and effects. *Acta Mater.*, 55(3):1067–1081.

[2] Vorontsov V.A., Shen C., Wang Y., Dye D., and Rae C.M.F., 2010. Shearing of γ' precipitates by $a\langle 112\rangle$ dislocation ribbons in Ni-base superalloys: A phase field approach. *Acta Mater.*, 58(12):4110–4119.

[3] Pollock T.M. and Argon A.S., 1992. Creep resistance of CMSX-3 nickel-base superalloy single-crystals. *Acta Metall. Mater.*, 40(1):1–30.

[4] Vattre A., Devincre B., and Roos A., 2010. Orientation dependence of plastic deformation in nickel-based single crystal superalloys: Discrete-continuous model simulations. *Acta Mater.*, 58(6):1938–1951.

[5] Probst-Hein M., Dlouhy A., and Eggeler G., 1999. Interface dislocations in superalloy single crystals. *Acta Mater.*, 47(8):2497–2510.

[6] Matan N., Cox D.C., Rae C.M.F., and Reed R.C., 1999. On the kinetics of rafting in CMSX-4 superalloy single crystals. *Acta Mater.*, 47(7):2031–2045.

[7] Zhang J.X., Wang J.C., Harada H., and Koizumi Y., 2005. The effect of lattice misfit on the dislocation motion in superalloys during high-temperature low-stress creep. *Acta Mater.*, 53(17):4623–4633.

[8] Carry C. and Strudel J.L., 1977. Apparent and effective creep parameters in single crystals of a nickel base superalloy–I incubation period. *Acta Metall.*, 25(7):767–777.

[9] Svoboda J. and Lukas P., 1997. Modelling of recovery controlled creep in nickel-base superalloy single crystals. *Acta Mater*, 45(1):125–135.

[10] Epishin A. and Link T., 2004. Mechanisms of high-temperature creep of nickel-based superalloys under low applied stresses. *Philos. Mag.*, 84(19):1979–2000.

[11] Link T., Epishin A., Klaus M., Bruckner U., and Reznicek A., 2005. $\langle 100 \rangle$ Dislocations in nickel-base superalloys: Formation and role in creep deformation. *Mater. Sci. Eng. A*, 405(1-2):254–265.

[12] Sarosi P.M., Srinivasan R., Eggeler G.F., Nathal M.V., and Mills M.J., 2007. Observations of $a \langle 010 \rangle$ dislocations during the high-temperature creep of Ni-based superalloy single crystals deformed along the $[001]$ orientation. *Acta Mater*, 55(7):2509–2518.

[13] Field R.D., Pollock T.M., and Murphy W.H., 1992. The development of γ/γ' interfacial dislocation networks during creep in Ni-base superalloys. In Antolovich, S. D. and Stusrud, R. W. and Mackay, R. A. and Anton, D. L. and Khan, T. and Kissinger, R. D. and Klarstrom, D. L. (Ed.), *Superalloys 1992*, pages 557–566. The Minerals, Metals and Materials Society, Warrendale, PA.

[14] Tian S.G., Zhou H.H., Zhang J.H., Yang H.C., Xu Y.B., and Hu Z.Q., 2000. Formation and role of dislocation networks during high temperature creep of a single crystal nickel-base superalloy. *Mater. Sci. Eng. A*, 279(1-2):160–165.

[15] Jacome L.A., Noertershaeuser P., Heyer J.K., Lahni A., Frenzel J., Dlouhy A., Somsen C., and Eggeler G., 2013. High-temperature and low-stress creep anisotropy of single-crystal superalloys. *Acta Mater.*, 61(8):2926–2943.

[16] Carry C., Dermarkar S., StrudeL J.L., and Wonsiewicz B.C., 1979. Internal-stresses due to dislocation walls around second phase particles. *Metall. Trans. A*, 10(7):855–860.

[17] Dlouhy A., Probst-Hein M., and Eggeler G., 2001. Static dislocation interactions in thin channels between cuboidal particles. *Mater. Sci. Eng. A*, 309(SI):278–282.

[18] Carry C. and StrudeL J.L., 1978. Apparent and effective creep parameters in single-crystals of a nickel base superalloy–II secondary creep. *Acta Metall.*, 26(5):859–870.

[19] Zhu Z., Basoalto H., Warnken N., and Reed R.C., 2012. A model for the creep deformation behaviour of nickel-based single crystal superalloys. *Acta Mater.*, 60(12):4888–4900.

[20] Kubin L.P., Canova G., Condat M., Devincre B., Pontikis V., and Brechet Y., 1992. Dislocation microstructures and plastic flow: a 3D simulation. *Solid State Phenomena*, 23-24:455–72.

[21] Zbib H.M., Rhee M., and Hirth J.P., 1998. On plastic deformation and the dynamics of 3D dislocations. *Int. J. Mech. Sci.*, 40(2-3):113–127.

[22] Schwarz K.W., 1999. Simulation of dislocations on the mesoscopic scale. I. Methods and examples. *J. Appl. Phys.*, 85(1):108–119.

[23] Ghoniem N.M., Tong S.H., and Sun L.Z., 2000. Parametric dislocation dynamics: A thermodynamics-based approach to investigations of mesoscopic plastic deformation. *Phys. Rev. B*, 61(2):913–927.

[24] Weygand D., Friedman L.H., Van der Giessen E., and Needleman A., 2002. Aspects of boundary-value problem solutions with three-dimensional dislocation dynamics. *Modelling Simul. Mater. Sci. Eng.*, 10(4):437–468.

[25] Arsenlis A., Cai W., Tang M., Rhee M., Oppelstrup T., Hommes G., Pierce T.G., and Bulatov V.V., 2007. Enabling strain hardening simulations with dislocation dynamics. *Modelling Simul. Mater. Sci. Eng.*, 15(6):553–595.

[26] Madec R., Devincre B., Kubin L.P., Hoc T., and Rodney D., 2003. The role of collinear interaction in dislocation-induced hardening. *Science*, 301(5641):1879–1882.

[27] Bulatov V.V., Hsiung L.L., Tang M., Arsenlis A., Bartelt M.C., Cai W., Florando J.N., Hiratani M., Rhee M., Hommes G., Pierce T.G., and de la Rubia T.D., 2006. Dislocation multi-junctions and strain hardening. *Nature*, 440(7088):1174–1178.

[28] Wu C.C., Chung P.W., Aubry S., Munday L.B., and Arsenlis A., 2013. The strength of binary junctions in hexagonal close-packed crystals. *Acta Mater.*, 61(9):3422–3431.

[29] Akasheh F., Zbib H.M., Hirth J.P., Hoagland R.G., and Misra A., 2007. Dislocation dynamics analysis of dislocation intersections in nanoscale metallic multilayered composites. *J. Appl. Phys.*, 101(8).

[30] Rao S.I., Dimiduk D.M., Parthasarathy T.A., Uchic M.D., Tang M., and Woodward C., 2008. Athermal mechanisms of size-dependent crystal flow gleaned from three-dimensional discrete dislocation simulations. *Acta Mater.*, 56(13):3245–3259.

[31] Tang H., Schwarz K.W., and Espinosa H.D., 2008. Dislocation-source shutdown and the plastic behavior of single-crystal micropillars. *Phys. Rev. Lett.*, 100(18).

[32] Motz C., Weygand D., Senger J., and Gumbsch P., 2009. Initial dislocation structures in 3-D discrete dislocation dynamics and their influence on microscale plasticity. *Acta Mater.*, 57(6):1744–1754.

[33] Liu B., Raabe D., Eisenlohr P., Roters F., Arsenlis A., and Hommes G., 2011. Dislocation interactions and low-angle grain boundary strengthening. *Acta Mater.*, 59(19):7125–7134.

[34] Liu B., Eisenlohr P., Roters F., and Raabe D., 2012. Simulation of dislocation penetration through a general low-angle grain boundary. *Acta Mater.*, 60(13-14):5380–5390.

[35] Caillard D. and Martin J.L., 2003. *Thermally Activated Mechanisms in Crystal Plasticity*. Pergamon Press, Amsterdam.

[36] Friedel J., 1964. *Dislocations*. Pergamon Press, Oxford.

[37] Hirth J.P. and Lothe J., 1982. *Theory of Dislocations*. Wiley, New York.

[38] Mordehai D., Clouet E., Fivel M., and Verdier M., 2008. Introducing dislocation climb by bulk diffusion in discrete dislocation dynamics. *Philos. Mag.*, 88(6):899–925.

[39] Bako B., Clouet E., Dupuy L.M., and Bletry M., 2011. Dislocation dynamics simulations with climb: kinetics of dislocation loop coarsening controlled by bulk diffusion. *Philos. Mag.*, 91(23):3173–3191.

[40] Clouet E., 2011. Predicting dislocation climb: Classical modeling versus atomistic simulations. *Phys. Rev. B*, 84(9).

[41] Davoudi K.M., Nicola L., and Vlassak J.J., 2012. Dislocation climb in two-dimensional discrete dislocation dynamics. *J. Appl. Phys.*, 111(10).

[42] Keralavarma S.M., Cagin T., Arsenlis A., and Benzerga A.A., 2012. Power-Law Creep from Discrete Dislocation Dynamics. *Phys. Rev. Lett.*, 109(26).

[43] Danas K. and Deshpande V.S., 2013. Plane-strain discrete dislocation plasticity with climb-assisted glide motion of dislocations. *Modelling Simul. Mater. Sci. Eng.*, 21(4).

[44] Xiang Y. and Srolovitz D.J., 2006. Dislocation climb effects on particle bypass mechanisms. *Philos. Mag.*, 86(25-26):3937–3957.

[45] Quek S.S., Xiang Y., and Srolovitz D.J., 2011. Loss of interface coherency around a misfitting spherical inclusion. *Acta Mater.*, 59(14):5398 – 5410.

[46] Documentation of ParaDiS v2.5.1.

[47] Raabe D., 1998. On the consideration of climb in discrete dislocation dynamics. *Philos. Mag. A*, 77(3):751–759.

[48] Mohles V., 2001. Orowan process controlled dislocation glide in materials containing incoherent particles. *Mater. Sci. Eng. A*, 309(SI):265–269.

[49] Rao S.I., Parthasarathy T.A., Dimidukz D.M., and Hazzledineyy P.M., 2004. Discrete dislocation simulations of precipitation hardening in superalloys. *Philos. Mag.*, 84(30):3195–3215.

[50] Yashiro K., Kurose F., Nakashima Y., Kubo K., Tomita Y., and Zbib H.M., 2006. Discrete dislocation dynamics simulation of cutting of γ' precipitate and interfacial dislocation network in Ni-based superalloys. *Int. J. Plast.*, 22(4):713–723.

[51] Vattre A., Devincre B., and Roos A., 2009. Dislocation dynamics simulations of precipitation hardening in Ni-based superalloys with high γ' volume fraction. *Intermetallics*, 17(12):988–994.

[52] Huang M., Zhao L., and Tong J., 2012. Discrete dislocation dynamics modelling of mechanical deformation of nickel-based single crystal superalloys. *Int. J. Plast.*, 28(1):141–158.

[53] Glatzel U. and Feller-Kniepmeier M., 1989. Calculations of internal-stresses in the γ/γ' microstructure of a nickel-base superalloy with high volume fraction of γ'-phase. *Scripta Metall.*, 23(11):1839–1844.

[54] Ganghoffer J.F., Hazotte A., Denis S., and Simon A., 1991. Finite-element calculation of internal mismatch stresses in a single-crystal nickel-base superalloy. *Scripta Metall. Mater.*, 25(11):2491–2496.

[55] Muller L., Glatzel U., and Feller-Kniepmeier M., 1992. Modeling thermal misfit stresses in nickel-base superalloys containing high-volume fraction of γ-phase. *Acta Metall. Mater.*, 40(6):1321–1327.

[56] Pollock T.M. and Argon A.S., 1994. Directional coarsening in nickel-base single-crystals with high-volume fractions of coherent precipitates. *Acta Metall. Mater.*, 42(6):1859–1874.

[57] Pollock T.M. and Field R.D., 2002. Dislocations and high-temperature plastic deformation of superalloy single crystals. In F.R.N. Nabarro and M.S. Duesbery (Eds.), *Dislocations in solids, vol. 11*, pages 547–618. North Holland, Amsterdam.

[58] Srinivasan R., Eggeler G., and Mills M., 2000. γ'-cutting as rate-controlling recovery process during high-temperature and low-stress creep of superalloy single crystals. *Acta Mater.*, 48(20):4867 – 4878.

[59] Groves G.W. and Kelly A., 1962. Climb of dislocations in magnesium oxide. *J. Appl. Phys.*, 33(1):456–460.

[60] Phillips D., Pletka B., Heuer A., and Mitchell T., 1982. An improved model of break-up of dislocation dipoles into loops: Application to sapphire. *Acta Metall.*, 30(2):491 – 498.

[61] Lagerlf K., Mitchell T., and Heuer A., 1989. Energetics of the break-up of dislocation dipoles into prismatic loops. *Acta Metall.*, 37(12):3315 – 3325.

[62] Gao Y., Zhuang Z., Liu Z., You X., Zhao X., and Zhang Z., 2011. Investigations of pipe-diffusion-based dislocation climb by discrete dislocation dynamics. *Int. J. Plast.*, 27(7):1055 – 1071.

[63] Reed R.C., Matan N., Cox D.C., Rist M.A., and Rae C.M.F., 1999. Creep of CMSX-4 superalloy single crystals: effects of rafting at high temperature. *Acta Mater.*, 47(12):3367 – 3381.

[64] Eggeler G. and Dlouhy A., 1997. On the formation of $\langle 010 \rangle$-dislocations in the γ'-phase of superalloy single crystals during high temperature low stress creep. *Acta Mater.*, 45(10):4251 – 4262.